

# Suppressed self-diffusion of nanoscale constituents of a complex liquid

Christian P. N. Tanner,<sup>†</sup> Vivian R. K. Wall,<sup>†</sup> Mumtaz Gababa,<sup>†</sup> Joshua Portner,<sup>‡</sup> Ahhyun Jeong,<sup>‡</sup> Matthew J. Hurley,<sup>¶,§</sup> Nicholas Leonard,<sup>¶</sup> Jonathan G. Raybin,<sup>†</sup> James K. Utterback,<sup>†,||</sup> Ahyoung Kim,<sup>†,⊥</sup> Andrei Fluerașu,<sup>#</sup> Yanwen Sun,<sup>@</sup> Johannes Möller,<sup>△</sup> Alexey Zozulya,<sup>△</sup> Wonhyuk Jo,<sup>△</sup> Anders Madsen,<sup>△</sup> Dmitri V. Talapin,<sup>‡,▽</sup> Samuel W. Teitelbaum,<sup>¶</sup> and Naomi S. Ginsberg<sup>\*,†,††,‡‡,¶¶,§§,||||</sup>

<sup>†</sup>*Department of Chemistry, University of California, Berkeley, CA 94720, USA*

<sup>‡</sup>*Department of Chemistry, James Franck Institute, and Pritzker School of Molecular Engineering, University of Chicago, Chicago, IL 60637, USA*

<sup>¶</sup>*Department of Physics, Arizona State University, Tempe, AZ 85287, USA*

<sup>§</sup>*Present Address: Department of Physics, Stanford University, Stanford, CA 94305, USA*

<sup>||</sup>*Present Address: Sorbonne Université, CNRS, Institut des NanoSciences de Paris, INSP, 75005 Paris, France*

<sup>⊥</sup>*Present Address: California Institute of Technology, Pasadena, CA 91125, USA*

<sup>#</sup>*Brookhaven National Laboratory, NSLS-II, Upton, NY 11973, USA*

<sup>@</sup>*Linac Coherent Light Source, SLAC National Accelerator Laboratory, Menlo Park, CA 94025, USA*

<sup>△</sup>*European X-ray Free-Electron Laser Facility, Holzkoppel 4, 22869 Schenefeld, Germany*

<sup>▽</sup>*Center for Nanoscale Materials, Argonne National Laboratory, Argonne, IL 60517, USA*

<sup>††</sup>*Department of Physics, University of California, Berkeley, CA 94720, USA*

<sup>‡‡</sup>*Molecular Biophysics and Integrated Bioimaging Division, Lawrence Berkeley National Laboratory, Berkeley, CA 94720, USA*

<sup>¶¶</sup>*Materials Sciences and Chemical Sciences Division, Lawrence Berkeley National Laboratory, Berkeley, CA 94720, USA*

<sup>§§</sup>*Kavli Energy NanoSciences Institute, University of California, Berkeley, CA 94720, USA*

<sup>||||</sup>*STROBE, NSF Science & Technology Center, Berkeley, CA 94720, USA*

E-mail: nsginsberg@berkeley.edu

## Abstract

The ability to understand and ultimately control the transformations and properties of various nanoscale systems, from proteins to synthetic nanomaterial assemblies, hinges on the ability to directly elucidate their dynamics on their characteristic length and time scales. Here, we use MHz X-ray photon correlation spectroscopy (XPCS) to directly elucidate the characteristic microsecond-dynamics of den-

sity fluctuations of semiconductor nanocrystals (NCs), not only in a colloidal dispersion but also in a liquid phase consisting of densely packed, yet mobile, NCs with no long-range order. By carefully disentangling X-ray induced effects, we find the wavevector-dependent fluctuation rates in the liquid phase are suppressed relative to those in the colloidal phase and to those in experiments and hydrodynamic theories of densely packed repulsive particles. We show that the suppressed rates are due to a

substantial decrease in the self-diffusion of NCs in the liquid phase, which we attribute to explicit attractive interactions. Via comparison with simulations, we find that the extracted strength of the attractions explains the stability of the liquid phase, in contrast to the gelation observed via XPCS in many other charged colloidal systems. This work opens the door to elucidating fast, condensed phase dynamics in a variety of complex fluids and other nanoscale soft matter systems, such as densely packed proteins and non-equilibrium self-assembly processes.

### Keywords:

complex fluids, hydrodynamics, nanocrystals, coherent X-ray scattering, liquid phase dynamics, correlation spectroscopy

Understanding the dynamics of systems on their characteristic time- and length scales enables control over important system properties. For example, the fluctuations of microscopic parameters of a system, such as the density field or velocity of a particle, encode transport properties of the system like the diffusion coefficient.<sup>1</sup> Knowledge of the dependence of transport properties on experimentally accessible control parameters thus enables direct control over system properties. One important example of this connection is understanding how the diffusivity of particles in a colloidal suspension changes as a function of the interactions between the particles and their concentration.<sup>2–4</sup> While much work has gone into understanding the hydrodynamic, i.e., solvent-mediated, interactions of model systems, such as ensembles of repulsive spheres,<sup>5–9</sup> the interactions between particles in complex fluids (nanocrystal assemblies, proteins, polymers, etc.) are often more complicated and difficult to predict due to the many-body nature of their interactions. Understanding and ultimately controlling the interactions between particles in these complex fluids requires directly elucidating their dynamics on their characteristic time- and length scales.

Measuring the dynamics of many complex fluid systems is challenging due to their small length scales (nm) and fast time scales ( $\mu$ s). Typically, the dynamics associated with translational, vibrational, or rotational motion of micron-scale particles are measured in the time-domain with optical scattering or optical microscopy techniques.<sup>10–15</sup> For atomic systems, these dynamics are measured in the frequency domain using inelastic X-ray or neutron scattering techniques that are limited to ns or shorter time scales.<sup>16</sup> MHz X-ray photon correlation spectroscopy (XPCS) at the European X-ray free electron laser (XFEL) offers the ability to measure dynamics on microsecond time scales,<sup>17,18</sup> filling an important time scale gap present with previously available techniques. XPCS is a time-domain coherent X-ray scattering technique that measures density fluctuations in reciprocal space.<sup>6,16,19–23</sup> In order to generate high enough signal-to-noise ratio in the scattered signal, high intensity X-rays are required, which in turn can damage a sample and influence its dynamics.<sup>9,18,24</sup> As a result, special care is required to understand and minimize X-ray induced effects when using XPCS.<sup>25</sup>

Despite the fast time- and short length scales of nanoscale systems, we directly elucidate the dynamics associated with density fluctuations of few-nanometer-diameter charged semiconductor nanocrystals (NCs) as a function of their volume fraction and interaction strength using MHz XPCS. By changing the ionic strength of the dispersing solution, we tune the electrostatic repulsion between the charged NCs, thereby controlling the strength of their interactions. As a result, we are able to generate both stable colloidal and liquid phases.<sup>26,27</sup> The liquid phase consists of densely packed, mobile NCs with no long-range order. By developing analysis methods for the X-ray scattering data, we carefully disentangle the intrinsic dynamics of the NCs in the colloidal and liquid phases from the X-ray induced effects on the system. In combination with theoretical methods, we extract the self-diffusion coefficient<sup>1</sup> of the NCs as a function of their volume fraction and interaction strength and find that the self-diffusion coefficient of the liquid-phase NCs is

suppressed relative to that of hard spheres<sup>7</sup> and charged spheres<sup>7</sup> at the same volume fraction. We show that this suppression can be explained through explicit attractive interactions between the NCs, and we extract the strength of their interactions via direct comparison with simulations. The strength of this attraction ( $\sim 1.5 k_B T$ ) explains the stability of this liquid phase and why these NCs avoid arrest or gelation following quenches from the colloidal phase, which has important implications for the assembly of these NCs into ordered arrays for optoelectronic applications.<sup>26–33</sup> The combination of experiment, analysis, theory, and simulation enables us to determine the transport properties and interactions of NCs in this system, and similar approaches should be able to directly elucidate similar properties of other complex fluids, such as polymer systems<sup>34,35</sup> and proteins under physiological, cellular conditions.<sup>24,36</sup>

***Disentangling the intrinsic dynamics of colloidal and liquid-phase charged NCs.*** To determine the interactions between NCs in complex fluid phases, we study  $5.8 \pm 0.3$  nm diameter PbS NCs coated with  $K_4Sn_2S_6$  ligands dispersed in a mixture of N-methylformamide (NMF) and N,N-dimethylformamide (DMF) at volume fractions of  $\sim 0.001$  to  $0.02$ .<sup>26</sup> In addition to studying the NCs in the colloidal phase, we generate a NC liquid phase consisting of densely packed NCs by quenching the system via addition of excess  $K_3AsS_4$  salt solution. The salt screens the electrostatic repulsion stabilizing the NCs in the colloidal phase and results in overall attractive interactions between NCs.<sup>27</sup> To measure the structure and dynamics of NCs in the colloidal and liquid phases, we use MHz XPCS at the Materials Imaging and Dynamics (MID) instrument at the European XFEL (**Figures 1, S1**). The NC solutions in thin-walled borosilicate capillaries scatter X-rays generated from pulse trains consisting of  $N_{\text{train}} = 50$  ultrafast ( $\sim 50$  fs pulse width), spatially coherent X-ray pulses at a 2.2 MHz repetition rate onto the adaptive gain integrated pixel detector<sup>37</sup> (AGIPD) located 7 m from the sample plane. Examples of detector images are shown in **Figure 2a**. By azimuthally integrating the detector images, we

obtain one-dimensional SAXS patterns,  $I(q)$ , which describe the intensity of scattered X-rays as a function of wavevector transfer,  $q$  (**Figure 2b, Figure S2**). By fitting the SAXS patterns to models of colloidal and liquid phases (see **Methods**), we extract the size distribution of the NCs as well as the volume fraction of NCs in the liquid phase, which is 0.3 for the example in **Figure 2b**.

To obtain the characteristic dynamics associated with density fluctuations of the NCs, we calculate two-time correlation functions,  $C(q, t_1, t_2)$ , according to

$$C(q, t_1, t_2) = \frac{\langle \delta I(q, t_1) \delta I(q, t_2) \rangle_{\text{sp}}}{\langle I(q, t_1) \rangle_{\text{sp}} \langle I(q, t_2) \rangle_{\text{sp}}},$$

where  $\delta I(q, t_1) = I(q, t_1) - \langle I(q, t_1) \rangle_{\text{sp}}$  and  $\langle \dots \rangle_{\text{sp}}$  denotes an average over speckles in the same region of interest on the detector corresponding to the value of  $q$ . The two-time correlation functions  $C(q, t_1, t_2)$  were calculated over the 50 pulses within each pulse train and then averaged across all pulse trains for each sample experiment (see **Methods**). Examples of  $C(q, t_1, t_2)$  for the NCs in the colloidal and liquid phases are shown in **Figure 3a**. The distance along the diagonal of the plots in **Figure 3a** indicates the age,  $t$ , of the sample within the pulse train, where  $t = (t_1 + t_2)/2$ . In other words,  $t$  indicates how many pulses the sample has sustained. Following the value of  $C(q, t_1, t_2)$  as it extends perpendicular to the diagonal provides the decay of the correlation function at a fixed age (fixed value of  $t$ ). The antidiagonal decay of  $C(q, t_1, t_2)$  is also seen to depend on  $t$ , indicating that the sample dynamics are changing as more X-ray pulses within a pulse train have interacted with the sample. To quantify these dynamics, we calculate autocorrelation functions,  $g^{(2)}$ , from  $C(q, t_1, t_2)$  at a fixed average sample age,  $\bar{t}$ . In other words, we compute  $g^{(2)}(q, \tau, \bar{t}) - 1 = \overline{C(q, t_1, t_2)}$ , where  $\tau = t_2 - t_1$  and the overbar on the two-time correlation function indicates an average over times  $t_1$  and  $t_2$  at constant  $\bar{t}$ , i.e., averaging the terms in  $C(q, t_1, t_2)$  along lines parallel to the  $t_1 = t_2$  diagonal with the constraint that the average value of  $(t_1 + t_2)/2$  of all of the

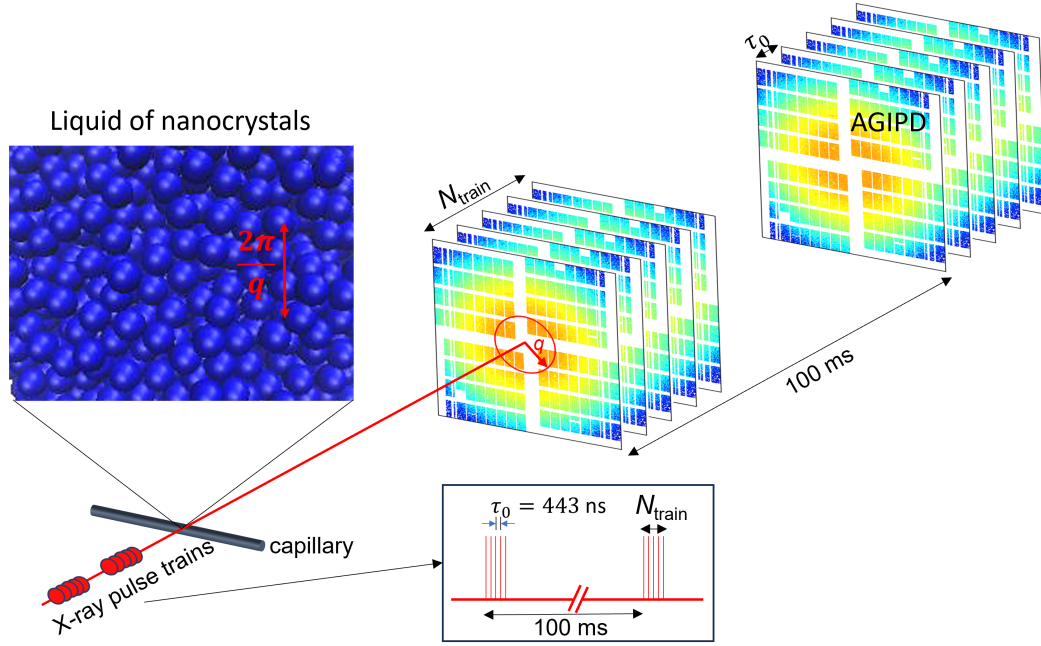


Figure 1: Schematic of MHz XPCS experiment. Ultrafast X-ray pulses are delivered to the sample consisting of a solution of NCs in a glass capillary. As the NCs fluctuate in solution, they scatter the X-rays onto the AGIPD detector that is timed to the incident X-ray pulses. The X-ray pulses are structured in pulse “trains,” consisting of  $N_{\text{train}}$  pulses at a 2.2 MHz repetition rate. In this schematic,  $N_{\text{train}} = 5$ , but in the experiments,  $N_{\text{train}} = 50$ . The first pulse in each pulse train is separated by 100 ms from the first pulse in the preceding pulse train. Correlation analysis is performed within each pulse train and then averaged over the  $\sim 100$ s of pulse trains within a measurement.

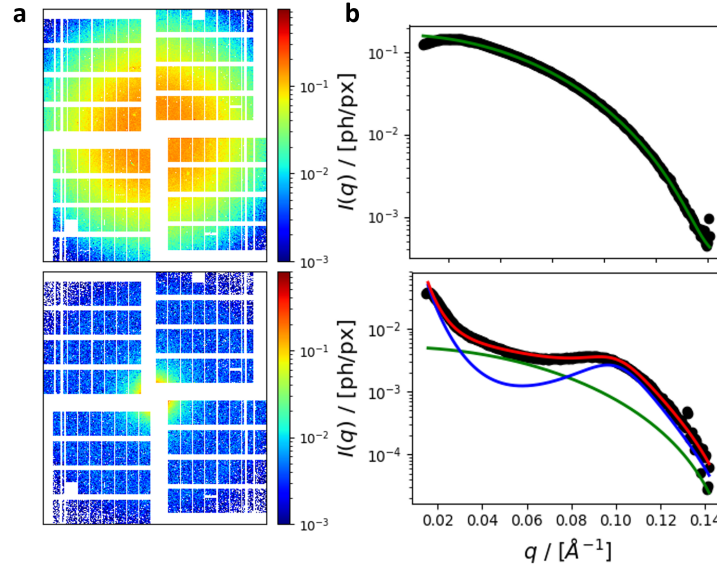


Figure 2: Static scattering of NCs in colloidal and liquid phases. **a.** Two-dimensional images on the AGIPD at European XFEL of scattering from NCs in the colloidal (top) and quenched (bottom) phases. **b.** Background-subtracted one-dimensional SAXS patterns,  $I(q)$ , of NCs in the colloidal (top) and quenched (bottom) phases (black data points). Fits (red) of colloidal (green) and liquid (blue) models to the SAXS pattern are shown as solid curves.

points used in the overbar average is constant. Autocorrelation functions for a series of values of  $q$  using averages over the first 10 X-ray pulses ( $0 \leq t \leq 8.86 \mu\text{s}$ ) in each pulse train corresponding to  $\bar{t} = 4.43 \mu\text{s}$  are shown via the points plotted in **Figure 3b**, each set of which is fit to a decaying exponential function (see below). The autocorrelation functions of the colloidal and liquid phases decay faster at higher  $q$  values, and they decay more slowly in the liquid phase than the colloidal phase. We ascribe the dynamics of the quenched state to the NCs in the liquid phase since the scattering from the liquid phase is  $\sim 1$  order of magnitude larger than that of the colloidal phase at the  $q$  values over which the correlation analysis was performed. We were not able to obtain useful autocorrelation functions at  $q$  values larger than  $\sim 0.030 \text{ \AA}^{-1}$  in the colloidal phase due to the decorrelation rates of the autocorrelation functions exceeding the instrumental limitation set by the X-ray pulse repetition rate of 2.2 MHz. We were unable to obtain meaningful autocorrelation functions for the liquid phase at higher  $q$  values due to the  $q^{-4}$  drop off in signal strength.

The autocorrelation functions vary as a function of  $\bar{t}$  (see **Figure S3a**). To extract the rate at which density fluctuations decorrelate, we fit an exponential model,<sup>38</sup>  $g^{(2)}(q, \tau, \bar{t}) = 1 + \beta(q) \exp[-2\Gamma(q, \bar{t})\tau]$  (solid curves in **Figure 3b**), to the autocorrelation functions and obtain  $\Gamma(q, \bar{t})$  (see **Methods** for more information). The speckle contrast,  $\beta(q)$ , in the fits in **Figure 3** is fixed based on the average of the direct calculation of the speckle contrast, i.e.,  $C(q, t_1, t_1)$ , of hundreds of individual images (see **Methods**). To obtain the decorrelation rate associated with the unperturbed NC dynamics, we extrapolate  $\Gamma(q, \bar{t})$  to  $\bar{t} \rightarrow 0$  (**Figure S3b**). The experimentally-determined rates,  $\Gamma(q, \bar{t} = 4.43 \mu\text{s})$  (open circles) and  $\Gamma(q, \bar{t} \rightarrow 0)$  (closed circles), are shown in **Figure 3c** in relation to the static structure factor,  $S^i(q) = \frac{1}{N} \langle \rho_q^i \rho_{-q}^i \rangle$ , for each of the colloidal ( $i = c$ ) and liquid ( $i = \ell$ ) phases, where  $N$  is the total number of NCs in the X-ray beam and  $\rho_q^i$  are the Fourier components of the NC density:  $\rho_q^i = \sum_n e^{-i\mathbf{q} \cdot \mathbf{r}_n^i}$  for location of NC  $n$  in phase

$i$ ,  $\mathbf{r}_n^i$ . Here,  $S^c(q)$  and  $S^\ell(q)$  describe the modulation in the scattered X-ray intensity due to the spatial arrangement of NCs in the colloidal and liquid phases, respectively. We find  $S^c(q) = 1$  (**Figure 3c**, black data points), indicating the NCs are far apart and do not interact with one another in the colloidal phase, as expected. The liquid phase structure factor,  $S^\ell(q)$ , has a distinct peak at  $q \sim 0.1 \text{ \AA}^{-1}$  corresponding to a nearest-neighbor distance between NCs in the liquid phase of  $\sim 6.3 \text{ nm}$  (**Figure 3c**, blue data points). The decorrelation rates,  $\Gamma(q, \bar{t} \rightarrow 0)$  and  $\Gamma(q, \bar{t} = 4.43 \mu\text{s})$  are  $\sim 1$  order of magnitude larger for the colloidal phase than the liquid phase, and they show a similar  $q$ -dependence.

To quantitate these trends, we fit  $\Gamma(q, \bar{t} \rightarrow 0)$  to a quadratic function:<sup>39</sup>  $\Gamma(q, \bar{t} \rightarrow 0) = D_{\text{eff}}^i(q)q^2$  (solid red curves in **Figure 3c**), where  $D_{\text{eff}}^i(q)$  is an effective diffusion coefficient. We find  $\langle D_{\text{eff}}^c(q) \rangle_q = 57 \mu\text{m}^2/\text{s}$  for the NCs in the colloidal phase and  $5 \mu\text{m}^2/\text{s}$  for NCs in the liquid phase. To extract information about the diffusivity of NCs in the colloidal and liquid phases, we relate  $D_{\text{eff}}^i(q)$  to the hydrodynamic functions,  $H^c(q)$  and  $H^\ell(q)$ , via  $D_{\text{eff}}^i(q) = D_0 H^i(q)/S^i(q)$ .<sup>3,40</sup> Here,  $D_0$  is the self-diffusion coefficient of dilute NCs and

$$H^i(q) = \left\langle \frac{1}{ND_0q^2} \sum_{m,n=1}^N \mathbf{q} \cdot D_{mn}^i \cdot \mathbf{q} \exp[i\mathbf{q} \cdot (\mathbf{r}_m - \mathbf{r}_n)] \right\rangle,$$

where  $D_{mn}^i$  is a diffusivity tensor that relates the hydrodynamic force on NC  $n$  to the translational velocity of NC  $m$ . The function  $H^i(q)$  encodes the direct interparticle interactions between NCs as well as the hydrodynamic, i.e., solvent-mediated, interactions between NCs, and is a many-body function that depends on all of the NCs in the system. To extract  $H^i(q)$  from the experimental data, we use the measured structure factors of the colloidal ( $S^c(q)$ ) and liquid ( $S^\ell(q)$ ) phases, the fitted values of  $D_{\text{eff}}^i(q)$ , and  $D_0$  obtained from dynamic light scattering (DLS) measurements of the NCs at a volume fraction of 0.0002 (**Figure S4**). There is no evidence of hydrodynamic interactions between the NCs in the colloidal phase, as  $H^c(q)=1$  (**Figure 4a**, black data points). We

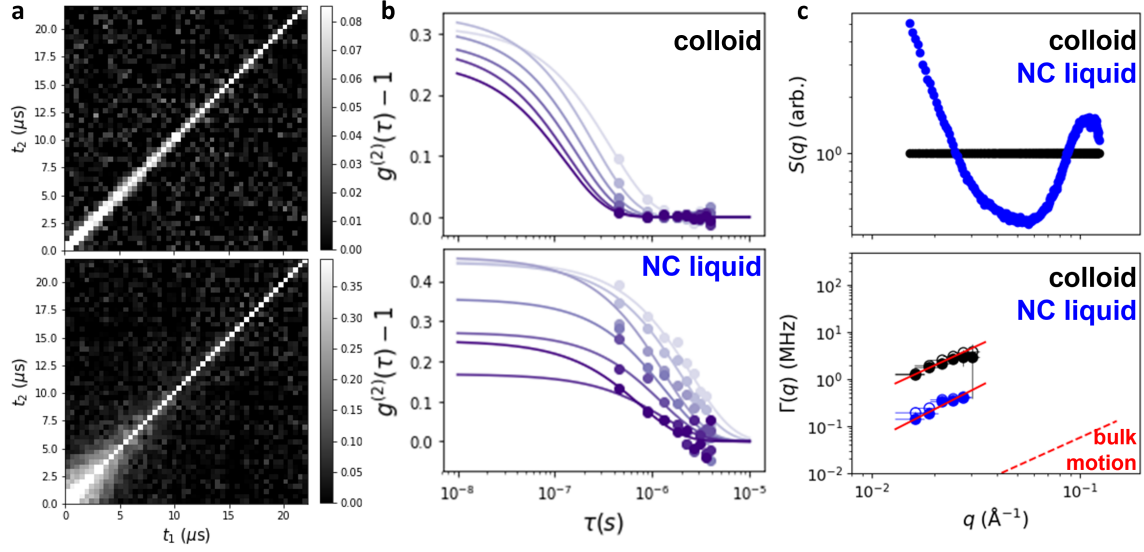


Figure 3: Microsecond dynamics associated with density fluctuations of NCs in colloidal and liquid phases. **a.** Two-time correlation functions,  $C(q, t_1, t_2)$ , for NCs in the colloidal (top) and liquid (bottom) phases at  $q = 0.016 \text{ \AA}^{-1}$ . **b.** Autocorrelation functions,  $g^{(2)}(q, \tau, \bar{t} = 4.43 \mu\text{s})$  as a function of  $q$  for NCs in the colloidal (top) and liquid (bottom) phases (purple data points). Momentum transfer  $q$  increases from light to dark purple. Solid curves are exponential fits to the data points. **c.** Structure factors,  $S^c(q)$  and  $S^\ell(q)$  (top), and decorrelation rates,  $\Gamma(q)$  (bottom), for NCs in the colloidal (black) and liquid (blue) phases. Open circles indicate  $\Gamma(q, \bar{t} = 4.43 \mu\text{s})$  and solid circles indicate  $\Gamma(q, \bar{t} \rightarrow 0)$ . Solid red curves are fits to  $\Gamma(q) = \langle D_{\text{eff}} \rangle q^2$ . Dashed red curve represents the decorrelation rate expected for bulk motion of  $\sim 300 \text{ nm}$  liquid droplets.

find the values of  $H^\ell(q)$  for the NCs in the liquid phase (blue data points in **Figure 4a**), however, are all below 1, indicating that the hydrodynamic interactions slow down the NC motion.

Despite the influence of the extremely bright X-ray pulses on the sample, we are able to disentangle the X-ray induced effects from the intrinsic NC dynamics. The decorrelation rates that we extract (**Figure 3c**) are not due to concentration fluctuations of NCs in the X-ray probe volume since these are  $q$ -independent contributions that occur on longer time scales (see **Figure S5**), and they are normalized out in the calculation of  $C(q, t_1, t_2)$ . In addition, the decorrelation rates increase with  $\bar{t}$  in a manner consistent with a first principles calculation developed by Lehmkuehler et al.<sup>18</sup> of the temperature profile surrounding the NCs due to absorption of X-rays (see **Figures S6, S7**). As a result, the NCs behave as if they are diffusing at a higher temperature, and our extrapolation procedure enables us to approximate the decorrelation rates in the absence of this temperature increase. Furthermore, using the  $\langle D_{\text{eff}}^c \rangle = 57 \mu\text{m}^2/\text{s}$  obtained for the NCs in the colloidal phase, the hydrodynamic diameter predicted through the Einstein-Smoluchowski relation is 6.2 nm. This value agrees with our range of expectations based on DLS of the NCs in the absence of X-ray irradiation (**Figure S4**) and the lattice constant of solid ordered arrays of NCs self-assembled in earlier work.<sup>27</sup> In addition, we estimate the size of individual liquid droplets to be at least  $\sim 2$  orders of magnitude larger than the individual NCs based on the low- $q$  features in  $I(q)$  (**Figure 2b**). As a result, the decorrelation rates we measure of the liquid phase are not due to bulk motion of liquid droplets, since these occur on much slower time scales (see **Figure 3c**, dashed red curve).

**Suppressed self-diffusion of liquid-phase NCs and stability of the liquid state.** Having determined the effective diffusion coefficient and hydrodynamic functions of NCs in the colloidal and liquid phases, it is possible to extract more precise information about the NC diffusivities. To do so, we can decompose  $H^i(q)$  into a self part (terms where  $m = n$ ) and distinct part ( $m \neq n$ ):

$H^i(q) = D_s^i/D_0 + H_d^i(q)$ , where  $D_s^i$  is the self-diffusion coefficient of the NCs in the system and  $H_d^i(q)$  is a  $q$ -dependent term that approaches 0 as  $q \rightarrow \infty$ . Since our experimental data and analysis cannot sufficiently approach  $q \rightarrow \infty$  to extract  $D_s^i/D_0$ , we instead use the  $\delta\gamma$ -method of Beenakur and Mazur<sup>41,42</sup> to approximate  $H^i(q)$  (solid curves in **Figure 4a**). Within the limitations of our  $q$  range we find  $H^\ell(q)$  for the NCs in the liquid phase are well-described by the  $\delta\gamma$ -method for  $H^\ell(q)$ , modified to have a  $D_s^\ell/D_0$  value of 0.23 (blue dashed line in **Figure 4a**). This value for  $D_s^\ell/D_0$  (**Figure 4b**, red heart) falls below the value predicted by the  $\delta\gamma$ -method as well as below experimentally verified values for hard spheres (**Figure 4b**, black curve) and charged spheres (**Figure 4b**, purple curve). Given that the NCs are only an order of magnitude larger than the surrounding ion and solvent molecules, the NC solvation shell fluctuations may well play a role in suppressing the NC self-diffusion, especially as compared to larger, e.g., micron-sized particles. Density-density correlations of higher order than the second-order ones that describe larger charged spheres may be essential to fully describe the dynamics of our nanoscale system. Nevertheless, we postulate that explicit attractive interactions between the NCs are predominantly responsible for the suppressed value of  $D_s^\ell/D_0$ . To test this hypothesis, we performed molecular dynamics (MD) simulations of NCs at the same volume fraction as the NCs in the liquid phase in the experiments. The NCs interact with a Lennard-Jones potential in which the strength of attractions is given by  $\epsilon$ . We computed the mean-squared displacement (MSD) of the NCs as a function of  $\epsilon$  (**Figure 4c**) and find that  $D_s/D_0$  decreases as  $\epsilon$  increases. The NCs in the simulation have the same value of  $D_s/D_0$  as those in the liquid phase in the experiments for  $\epsilon \sim 1.5 k_B T$ . This interaction strength between NCs is consistent with values predicted from simulations<sup>43</sup> of coarse-grained NCs and explains the stability of this liquid phase: in contrast to other NC systems following a quench out of the colloidal state,<sup>44,45</sup> the relatively shallow interaction strengths of the present NCs prevent their arrest in a glassy

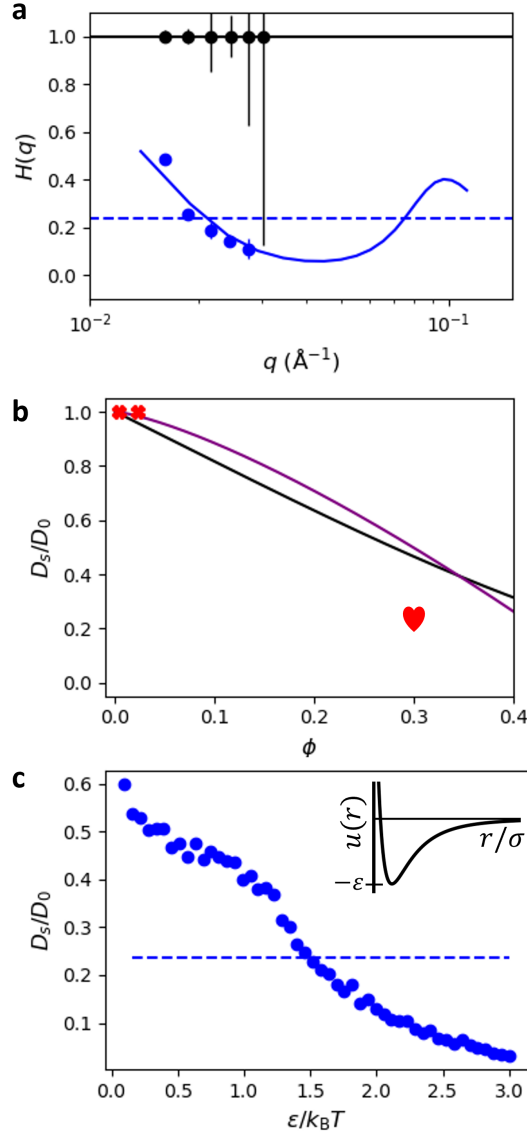


Figure 4: Hydrodynamic interactions of NCs as a function of their density and interaction strength. **a.** Hydrodynamic functions,  $H^i(q)$ , for NCs in the colloidal (black data points) and liquid (blue data points) phases. Solid curves are predictions of  $H^i(q)$  based on the  $\delta\gamma$ -method of Beenakur and Mazur with a modified self-diffusion coefficient for NCs in the liquid phase. Dashed blue curve represents the value of  $D_s^\ell/D_0$  that  $H^\ell(q)$  approaches as  $q \rightarrow \infty$ . **b.** Self-diffusion coefficient of NCs in the colloidal phase at two different volume fractions (red x's) and NCs in the liquid phase (red heart). Solid curves are the relationships between  $D_s^c/D_0$  and NC volume fraction ( $\phi^c$ ) for charged spheres<sup>7</sup> (purple curve) and hard spheres<sup>7</sup> (black curve). **c.** Self-diffusion coefficient of NCs interacting via a Lennard-Jones potential as a function of interaction strength,  $\epsilon$ , at a volume fraction of 0.3.



or gel-like state. This stability is crucial for the self-assembly of these NCs into ordered structures for optoelectronic applications.<sup>26,27</sup> In addition, the value of  $D_s^i/D_0$  for the NCs in the colloidal and liquid phases can be used in rate expressions<sup>27,46–48</sup> to predict and ultimately control the self-assembly kinetics, which is crucial to create defect-free structures. Further corroborating the experimental findings with simulations that also incorporate hydrodynamic effects<sup>7,49–51</sup> and can extend the  $q$  range over which to compare our system with models for  $H^i(q)$ , while challenging, will assist in refining our intuition about the source of the discrepancy between the properties of the liquid of NCs and  $\delta\gamma$ -method prediction.

In summary, we directly elucidate the dynamics associated with density fluctuations of charged semiconductor NCs in both a colloidal and liquid state using MHz XPCS. Excitingly, these studies occurred on the characteristic length- and time scales of the NC constituents, in contrast to XPCS of molecular or atomic liquids,<sup>52</sup> while focusing on an important nanosystem for bottom-up materials design. Upon isolating the intrinsic dynamics from X-ray-induced effects, we extract NC self-diffusion coefficients for both phases and thus find that NCs in the liquid phase have hindered motion beyond what is predicted for simple models. By comparing our results with a combination of analysis, theory, and simulation, we explain this finding via NC-NC attraction, which also explains the stability of the liquid state, as compared with the gelation of many other colloidal systems.

Investigating the microscopic source of the hydrodynamic interactions that we have discovered in this complex system of electrostatically stabilized NCs in their multivalent electrolyte solvent will enable a much greater degree of control over the interactions between charged NCs and other charged nanoscale systems. In addition to direct attractive interactions between NCs, ion rearrangements necessary to facilitate NC rearrangements also slow the NC diffusivity in the liquid state. Exploring higher order density-density correlations could aid in identifying the specific role of the ions and sol-

vent molecules in modulating the NC-NC attraction and the NC fluctuations. This work may lead to a deeper molecular understanding of the enigmatic solvation of the NCs<sup>53–55</sup> and their associated ability to crystallize, in addition to additional chemical and non-equilibrium strategies for forming unconventional complex liquids whose properties will also benefit from the lens of MHz XPCS. Future advances, especially in combination with advanced computation of force fields,<sup>56</sup> will lead to an unprecedented atomistic picture of complex, multiscale systems in which the specific role and interplay of nano-objects, surrounding ions, solvent molecules, and their fluctuations will be elucidated.

## Methods

**Sample preparation.** Stock solutions of  $5.8 \pm 0.3$  nm PbS NCs with  $K_4Sn_2S_6$  ligands in N-methylformamide (NMF) and 0.5 M  $K_3AsS_4$  salt in NMF were prepared following a procedure previously outlined.<sup>26,27</sup> In a nitrogen filled glovebox,  $\sim 50$   $\mu$ Ls of a solution of 5.8 nm PbS NCs with  $K_4Sn_2S_6$  ligands in mixtures of NMF and N,N-dimethylformamide (DMF) with varying amounts of  $K_3AsS_4$  salt were loaded into 0.9 mm outer-diameter borosilicate glass capillaries with 20-micron-thick walls. The capillaries were sealed and transported to the beamline for measurement.

**SAXS/XPCS experiments.** All SAXS/XPCS data were collected at the Materials Imaging and Dynamics (MID) instrument at the European XFEL. The X-ray photon energy was 12.3 keV and the sample-to-detector distance was 7 m. The X-ray beam size was  $\sim 2$ -3  $\mu$ m (**Figure S7**) and typical X-ray pulse energies at the sample position were  $\sim 2$ -3  $\mu$ J. Capillaries of PbS NCs at various concentrations dissolved in mixtures of N-methylformamide and N,N-dimethylformamide with varying amounts of  $K_3AsS_4$  salt were mounted at the beamline for data collection. The XFEL produced trains of ultrafast ( $\sim 50$  fs) spatially coherent X-ray pulses at a rate of 2.2 MHz. Each pulse train had 50 pulses. The first pulse of each train is de-

livered 0.1 s after the first pulse of the previous pulse train. Two-dimensional X-ray scattering data were collected and azimuthally integrated to obtain one-dimensional X-ray scattering patterns,  $I(q)$ .

**Modelling of SAXS patterns.** We model the background-subtracted scattered intensity as  $I(q) = I_{\text{colloid}}(q) + I_{\text{liquid}}(q)$ , where  $I_{\text{colloid}}(q)$  is the scattered intensity from dilute, polydisperse, hard spheres and  $I_{\text{liquid}}(q)$  is the scattered intensity from finite-sized liquid clusters of hard spheres.<sup>27,57</sup>  $I_{\text{colloid}}(q)$  is given by  $P(q)$ , the form factor for hard spheres of radius  $r$ , and has the explicit form  $P(q, r, \sigma, c_1) = c_1 \int_0^\infty |F(q, r)|^2 V(r)^2 P(r, \sigma) dr$ , where  $F(q, r) = 3[\sin(qr) - qr \cos(qr)]/(qr)^3$ ,  $V(r)$  is the volume of the hard sphere,  $P(r, \sigma)$  is a Gaussian probability distribution centered at  $r$  with standard deviation  $\sigma$ , and  $c_1$  is a number directly proportional to the number of hard spheres. For the liquid phase,  $I_{\text{liquid}}(q) = P(q)S_{\text{liquid}}(q)$ , where  $S_{\text{liquid}}(q)$  is given by the solution to the Ornstein-Zernicke equation using the Percus-Yevick closure relation for the case of hard spheres<sup>58-60</sup> plus an additional  $q^{-4}$  term to describe the scattering at low- $q$ . To explicitly compute  $I_{\text{colloid}}(q)$  and  $I_{\text{liquid}}(q)$  we use xrsdkit (<https://github.com/scattering-central/xrsdkit>). To extract  $S(q)$  from the experimentally measured SAXS patterns, we divide  $I(q)$  by the best-fit  $P(q)$  function.

**Correlation analysis.** Two-time correlation functions are defined via  $C_n(q, t_1, t_2) = \frac{\langle \delta I_n(q, t_1) \delta I_n(q, t_2) \rangle_{\text{sp}}}{\langle I_n(q, t_1) \rangle_{\text{sp}} \langle I_n(q, t_2) \rangle_{\text{sp}}}$ , where  $\delta I_n(q, t_1) = I_n(q, t_1) - \langle I_n(q, t_1) \rangle_{\text{sp}}$ ,  $\langle \dots \rangle_{\text{sp}}$  denotes an average over speckles in the same region of interest on the detector corresponding to the value of  $q$ , and  $I_n(q, t_1)$  and  $I_n(q, t_2)$  denote the scattered intensity in pulse train  $n$  as a function of times  $t_1$  and  $t_2$ , which take on values from 0 to 22.15  $\mu\text{s}$  (the duration of a single pulse train). The parameter  $n$  is the index of the pulse train and it goes from 1 to  $N$ , where  $N$  is the total number of pulse trains in a measurement.  $C(q, t_1, t_2, n)$  is calculated for each pulse train,  $n$ , in a measurement. Additional detector artifacts are removed<sup>61</sup> by subtracting  $XC = (XT_{-1} + XT_{+1})/2$  from

$C(q, t_1, t_2, n)$ , where  $XT_{-1} = (X_{-1} + X_{-1}^T)/2$  and  $XT_{+1} = (X_{+1} + X_{+1}^T)/2$ .  $X_{-1}$  and  $X_{+1}$  are cross correlation matrices calculated between intensities in neighboring pulse trains according to  $X_{-1} = \frac{\langle \delta I_{n-1}(q, t_1) \delta I_n(q, t_2) \rangle_{\text{sp}}}{\langle I_{n-1}(q, t_1) \rangle_{\text{sp}} \langle I_n(q, t_2) \rangle_{\text{sp}}}$  and  $X_{+1} = \frac{\langle \delta I_n(q, t_1) \delta I_{n+1}(q, t_2) \rangle_{\text{sp}}}{\langle I_n(q, t_1) \rangle_{\text{sp}} \langle I_{n+1}(q, t_2) \rangle_{\text{sp}}}$ .  $C(q, t_1, t_2)$  is calculated by averaging  $C(q, t_1, t_2, n) - XC$  over the several hundred pulse trains,  $N$ , for each sample:  $C(q, t_1, t_2) = \frac{1}{N} \sum_{n=1}^N C(q, t_1, t_2, n) - XC$ . The intensity-intensity autocorrelation function,  $g^{(2)}(q, \tau, \bar{t})$ , is calculated from  $C(q, t_1, t_2)$  via  $g^{(2)}(q, \tau, \bar{t}) - 1 = \overline{C(q, t_1, t_2)}$ , where  $\tau = t_2 - t_1$  and the overbar indicates an average over times  $t_1$  and  $t_2$  at constant average age,  $\bar{t}$ , where  $t = (t_1 + t_2)/2$ . We calculate intensity autocorrelation functions for different average ages,  $\bar{t}$ . The autocorrelation functions are fit to the following equation:  $g^{(2)}(q, \tau, \bar{t}) - 1 = \beta(q) \exp[-2\Gamma(q, \bar{t})\tau]$ , where  $\beta(q)$  is the speckle contrast and  $\Gamma(q, \bar{t})$  is the rate at which the autocorrelation function decays.  $\beta(q)$  in the fits in **Figure 3** is fixed based on the average of the direct calculation of the speckle contrast, i.e.,  $C(q, t_1, t_1)$ , of hundreds of individual images (see **Figure S8**).

**Approximations for  $H^i(q)$ .** We split  $H^i(q)$  into self ( $D_s^i/D_0$ ) and distinct ( $H_d^i(q)$ ) parts, where  $i=c, \ell$ . The  $\delta\gamma$ -method of Beenakker and Mazur to approximate  $H^i(q)$  is an effective medium approach based on a partial resummation of many body hydrodynamic interactions.<sup>7,41,42</sup> In the standard application of this method,  $D_s^i/D_0 = \frac{2}{\pi} \int_0^\infty dy [\frac{\sin y}{y}]^2 [1 + \phi^i S_{\gamma_0}(y)]^{-1}$ , where  $y = q\sigma$ ,  $\sigma$  is the diameter of the NCs,  $\phi^i$  is the volume fraction of NCs in phase  $i$ ,  $S_{\gamma_0}(y) = \frac{9}{2}[Si(2y)y^{-1} + \frac{1}{2} \cos(2y)y^{-2} + \frac{1}{4} \sin(2y)y^{-3} - (\sin y)^2 y^{-4} - 4(\sin y - y \cos y)^2 y^{-6}]$ , and  $Si(2y) = \int_0^{2y} dt \sin t/t$ .  $H_d^i(q) = \frac{3}{2\pi} \int_0^\infty dy' [\frac{\sin y'}{y'}]^2 [1 + \phi^i S_{\gamma_0}(y')]^{-1} \int_{-1}^1 d\mu (1 - \mu^2) [S^i(|\mathbf{q} - \mathbf{q}'|) - 1]$ , where  $\mu$  is the cosine of the angle between  $\mathbf{q}$  and  $\mathbf{q}'$ . The only input to these equations is the volume fraction of NCs,  $\phi^i$ , and the structure factors,  $S^i(q)$ . Higher order corrections to these approximations would require higher order correlation functions as input.

**Mean-squared displacement simulations.** Simulations of NCs were performed

with an underdamped Langevin dynamics in the  $NVT$  ensemble in a cubic periodic box using the LAMMPS software.<sup>62</sup> NCs were represented as 500 spherical particles with pairwise interactions given by a Lennard-Jones potential:  $u_{\text{LJ}}(r) = 4\epsilon[(\sigma/r)^{12} - (\sigma/r)^6]$ , where  $\epsilon$  is the depth of the interaction potential,  $\sigma$  is the diameter of the NCs, and  $r$  is the center to center distance between the NCs. At each value of  $\epsilon$ , the NCs are first equilibrated at a volume fraction of  $\phi = 0.3$  before calculating the mean-squared displacement. The mean-squared displacements (**Figure S9**) are fit to  $\text{MSD}(t) = 6D_s t$  to obtain the self-diffusion coefficient,  $D_s$ , of the NCs as a function of  $\epsilon$ .

## Conflicts of Interest

There are no conflicts to declare.

## Acknowledgments

This work was supported by the Office of Basic Energy Sciences (BES), US Department of Energy (DOE) (award no. DE-SC0019375). We acknowledge the European XFEL in Schenefeld, Germany, for provision of X-ray free electron laser beamtime at Scientific Instrument MID (Materials Imaging and Dynamics) and would like to thank the staff for their assistance. C.P.N.T. and V.R.K.W. were supported by the NSF Graduate Research Fellowship. J.K.U. was supported by an Arnold O. Beckman Postdoctoral Fellowship in Chemical Sciences from the Arnold and Mabel Beckman Foundation. D.T.L. was supported by an Alfred P. Sloan Research Fellowship. N.S.G. was supported by a David and Lucile Packard Foundation Fellowship for Science and Engineering and Camille and a Henry Dreyfus Teacher-Scholar Award.

## Supporting Information Available

Experimental details, modeling of SAXS patterns, age-dependent correlation analysis, DLS measurements, NC concentration fluctuations,

time-dependent heating model, characterization of X-ray beam size and speckle contrast, mean-squared displacement simulations.

## References

- (1) Chaikin, P. M.; Lubensky, T. C. *Principles of Condensed Matter Physics*; Cambridge University Press: Cambridge, 1995.
- (2) Jones, R. B.; Pusey, P. N. Dynamics of Suspended Colloidal Spheres. *Annual Review of Physical Chemistry* **1991**, *42*, 137–169, Publisher: Annual Reviews.
- (3) Nägele, G. On the dynamics and structure of charge-stabilized suspensions. *Physics Reports* **1996**, *272*, 215–372.
- (4) Brady, J. F. The rheological behavior of concentrated colloidal dispersions. *The Journal of Chemical Physics* **1993**, *99*, 567–581.
- (5) Ladd, A. J. C. Hydrodynamic transport coefficients of random dispersions of hard spheres. *The Journal of Chemical Physics* **1990**, *93*, 3484–3494.
- (6) Orsi, D.; Flueraşu, A.; Moussaïd, A.; Zontone, F.; Cristofolini, L.; Madsen, A. Dynamics in dense hard-sphere colloidal suspensions. *Physical Review E* **2012**, *85*, 011402, Publisher: American Physical Society.
- (7) Heinen, M.; Banchio, A. J.; Nägele, G. Short-time rheology and diffusion in suspensions of Yukawa-type colloidal particles. *The Journal of Chemical Physics* **2011**, *135*, 154504.
- (8) Westermeier, F.; Fischer, B.; Roseker, W.; Grübel, G.; Nägele, G.; Heinen, M. Structure and short-time dynamics in concentrated suspensions of charged colloids. *The Journal of Chemical Physics* **2012**, *137*, 114504.

- (9) Dallari, F. et al. Microsecond hydrodynamic interactions in dense colloidal dispersions probed at the European XFEL. *IUCrJ* **2021**, *8*, 775–783, Publisher: International Union of Crystallography.
- (10) Pusey, P. N.; Megen, W. v. Measurement of the short-time self-mobility of particles in concentrated suspension. Evidence for many-particle hydrodynamic interactions. *Journal de Physique* **1983**, *44*, 285–291, Publisher: Société Française de Physique.
- (11) van Megen, W.; Pusey, P. N. Dynamic light-scattering study of the glass transition in a colloidal suspension. *Physical Review A* **1991**, *43*, 5429–5441, Publisher: American Physical Society.
- (12) Gasser, U.; Weeks, E. R.; Schofield, A.; Pusey, P. N.; Weitz, D. A. Real-Space Imaging of Nucleation and Growth in Colloidal Crystallization. *Science* **2001**, *292*, 258–262, Publisher: American Association for the Advancement of Science.
- (13) Calderon, F. L.; Bibette, J.; Biais, J. Experimental Phase Diagrams of Polymer and Colloid Mixtures. *Europhysics Letters* **1993**, *23*, 653.
- (14) Savage, J. R.; Dinsmore, A. D. Experimental Evidence for Two-Step Nucleation in Colloidal Crystallization. *Physical Review Letters* **2009**, *102*, 198302.
- (15) Verhaegh, N. A. M.; van Duijnvelde, J. S.; Dhont, J. K. G.; Lekkerkerker, H. N. W. Fluid-Fluid Phase Separation in Colloid-Polymer Mixtures Studied with Small Angle Light Scattering and Light Microscopy. *Physica A: Statistical Mechanics and its Applications* **1996**, *230*, 409–436.
- (16) Sandy, A. R.; Zhang, Q.; Lurio, L. B. Hard X-Ray Photon Correlation Spectroscopy Methods for Materials Studies. *Annual Review of Materials Research* **2018**, *48*, 167–190, Publisher: Annual Reviews.
- (17) Grübel, G.; Stephenson, G. B.; Gutt, C.; Sinn, H.; Tschentscher, T. XPCS at the European X-ray free electron laser facility. *Nuclear Instruments and Methods in Physics Research Section B: Beam Interactions with Materials and Atoms* **2007**, *262*, 357–367.
- (18) Lehmkuhler, F. et al. Emergence of anomalous dynamics in soft matter probed at the European XFEL. *Proceedings of the National Academy of Sciences* **2020**, *117*, 24110–24116, Publisher: Proceedings of the National Academy of Sciences.
- (19) Sutton, M.; Mochrie, S. G. J.; Greytak, T.; Nagler, S. E.; Berman, L. E.; Held, G. A.; Stephenson, G. B. Observation of speckle by diffraction with coherent X-rays. *Nature* **1991**, *352*, 608–610, Publisher: Nature Publishing Group.
- (20) Flueraşu, A.; Sutton, M.; Dufresne, E. M. X-Ray Intensity Fluctuation Spectroscopy Studies on Phase-Ordering Systems. *Physical Review Letters* **2005**, *94*, 055501, Publisher: American Physical Society.
- (21) Shpyrko, O. G. X-ray photon correlation spectroscopy. *Journal of Synchrotron Radiation* **2014**, *21*, 1057–1064.
- (22) Sutton, M. A review of X-ray intensity fluctuation spectroscopy. *Comptes Rendus. Physique* **2008**, *9*, 657–667.
- (23) Grübel, G.; Madsen, A.; Robert, A. In *Soft Matter Characterization*; Borsali, R., Pecora, R., Eds.; Springer Netherlands: Dordrecht, 2008; pp 953–995.
- (24) Reiser, M. et al. Resolving molecular diffusion and aggregation of antibody proteins with megahertz X-ray free-electron laser pulses. *Nature Communications* **2022**, *13*, 5528.
- (25) Cao, Y.; Sheyfer, D.; Jiang, Z.; Madali, S.; You, H.; Wang, B.-X.; Ye, Z.-G.; Dufresne, E. M.; Zhou, H.; Stephenson, G. B.; Hruszkewycz, S. O. The Effect

- of Intensity Fluctuations on Sequential X-ray Photon Correlation Spectroscopy at the X-ray Free Electron Laser Facilities. *Crystals* **2020**, *10*, 1109.
- (26) Coropceanu, I. et al. Self-assembly of Nanocrystals into Strongly Electronically Coupled All-Inorganic Supercrystals. *Science* **2022**, *375*, 1422–1426.
  - (27) Tanner, C. P. N. et al. Enhancing nanocrystal superlattice self-assembly near a metastable liquid binodal. 2024; <http://arxiv.org/abs/2404.16808>, arXiv:2404.16808 [cond-mat].
  - (28) Boles, M. A.; Engel, M.; Talapin, D. V. Self-Assembly of Colloidal Nanocrystals: From Intricate Structures to Functional Materials. *Chemical Reviews* **2016**, *116*, 11220–11289.
  - (29) Murray, C. B.; Kagan, C. R.; Bawendi, M. G. Self-Organization of CdSe Nanocrystallites into Three-Dimensional Quantum Dot Superlattices. *Science* **1995**, *270*, 1335–1338.
  - (30) Shevchenko, E. V.; Talapin, D. V.; Kotoy, N. A.; O’Brien, S.; Murray, C. B. Structural Diversity in Binary Nanoparticle Superlattices. *Nature* **2006**, *439*, 55–59.
  - (31) Smith, D. K.; Goodfellow, B.; Smilgies, D.-M.; Korgel, B. A. Self-Assembled Simple Hexagonal AB<sub>2</sub> Binary Nanocrystal Superlattices: SEM, GISAXS, and Defects. *Journal of the American Chemical Society* **2009**, *131*, 3281–3290.
  - (32) Bian, K.; Choi, J. J.; Kaushik, A.; Clancy, P.; Smilgies, D.-M.; Hanrath, T. Shape-Anisotropy Driven Symmetry Transformations in Nanocrystal Superlattice Polymorphs. *ACS Nano* **2011**, *5*, 2815–2823.
  - (33) Santos, P. J.; Gabrys, P. A.; Zornberg, L. Z.; Lee, M. S.; Macfarlane, R. J. Macroscopic Materials Assembled from Nanoparticle Superlattices. *Nature* **2021**, *591*, 586–591.
  - (34) Nogales, A.; Flueraşu, A. X Ray Photon Correlation Spectroscopy for the study of polymer dynamics. *European Polymer Journal* **2016**, *81*, 494–504.
  - (35) Leheny, R. L. XPCS: Nanoscale motion and rheology. *Current Opinion in Colloid & Interface Science* **2012**, *17*, 3–12.
  - (36) Möller, J.; Sprung, M.; Madsen, A.; Gutt, C. X-ray photon correlation spectroscopy of protein dynamics at nearly diffraction-limited storage rings. *IUCrJ* **2019**, *6*, 794–803, Publisher: International Union of Crystallography.
  - (37) Henrich, B. et al. The adaptive gain integrating pixel detector AGIPD a detector for the European XFEL. *Nuclear Instruments and Methods in Physics Research Section A: Accelerators, Spectrometers, Detectors and Associated Equipment* **2011**, *633*, S11–S14.
  - (38) Madsen, A.; Leheny, R. L.; Guo, H.; Sprung, M.; Czakkel, O. Beyond simple exponential correlation functions and equilibrium dynamics in x-ray photon correlation spectroscopy. *New Journal of Physics* **2010**, *12*, 055001.
  - (39) Berne, B. J.; Pecora, R. *Dynamic Light Scattering: With Applications to Chemistry, Biology, and Physics*; Courier Corporation, 2000; Google-Books-ID: vBB54ABhmuEC.
  - (40) Pusey, P. N. The dynamics of interacting Brownian particles. *Journal of Physics A: Mathematical and General* **1975**, *8*, 1433.
  - (41) Beenakker, C.; Mazur, P. Self-diffusion of spheres in a concentrated suspension. *Physica A: Statistical Mechanics and its Applications* **1983**, *120*, 388–410.
  - (42) Beenakker, C. W. J.; Mazur, P. Diffusion of spheres in a concentrated suspension II. *Physica A: Statistical Mechanics and its Applications* **1984**, *126*, 349–370.

- (43) Haxton, T. K.; Hedges, L. O.; Whiteman, S. Crystallization and Arrest Mechanisms of Model Colloids. *Soft Matter* **2015**, *11*, 9307–9320.
- (44) K. Poon, W. C.; D. Pirie, A.; N. Pusey, P. Gelation in colloid–polymer mixtures. *Faraday Discussions* **1995**, *101*, 65–76, Publisher: Royal Society of Chemistry.
- (45) Kovalchuk, N. M.; Starov, V. M. Aggregation in colloidal suspensions: Effect of colloidal forces and hydrodynamic interactions. *Advances in Colloid and Interface Science* **2012**, *179–182*, 99–106.
- (46) Debenedetti, P. G. *Metastable Liquids: Concepts and Principles*; Princeton University Press, 1996; Vol. 1.
- (47) Nanev, C. N. In *Handbook of Crystal Growth (Second Edition)*; Nishinaga, T., Ed.; Elsevier: Boston, 2015; pp 315–358.
- (48) Uwaha, M. In *Handbook of Crystal Growth (Second Edition)*; Nishinaga, T., Ed.; Elsevier: Boston, 2015; pp 359–399.
- (49) Brady, J. F.; Bossis, G. Stokesian Dynamics. *Annual Review of Fluid Mechanics* **1988**, *20*, 111–157, Publisher: Annual Reviews.
- (50) Banchio, A. J.; Brady, J. F. Accelerated Stokesian dynamics: Brownian motion. *The Journal of Chemical Physics* **2003**, *118*, 10323–10332.
- (51) Phung, T. N.; Brady, J. F.; Bossis, G. Stokesian Dynamics simulation of Brownian suspensions. *Journal of Fluid Mechanics* **1996**, *313*, 181–207.
- (52) Hruszkewycz, S. O. et al. High Contrast X-ray Speckle from Atomic-Scale Order in Liquids and Glasses. *Physical Review Letters* **2012**, *109*, 185502, Publisher: American Physical Society.
- (53) Silvera Batista, C. A.; Larson, R. G.; Kotov, N. A. Nonadditivity of nanoparticle interactions. *Science* **2015**, *350*, 1242477, Publisher: American Association for the Advancement of Science.
- (54) Zhang, H.; Dasbiswas, K.; Ludwig, N. B.; Han, G.; Lee, B.; Vaikuntanathan, S.; Talapin, D. V. Stable colloids in molten inorganic salts. *Nature* **2017**, *542*, 328–331.
- (55) Kamysbayev, V.; Srivastava, V.; Ludwig, N. B.; Borkiewicz, O. J.; Zhang, H.; Ilavsky, J.; Lee, B.; Chapman, K. W.; Vaikuntanathan, S.; Talapin, D. V. Nanocrystals in Molten Salts and Ionic Liquids: Experimental Observation of Ionic Correlations Extending beyond the Debye Length. *ACS Nano* **2019**, *13*, 5760–5770.
- (56) Keith, J. A.; Vassilev-Galindo, V.; Cheng, B.; Chmiela, S.; Gastegger, M.; Müller, K.-R.; Tkatchenko, A. Combining Machine Learning and Computational Chemistry for Predictive Insights Into Chemical Systems. *Chemical Reviews* **2021**, *121*, 9816–9872.
- (57) Tanner, C. P. N.; Utterback, J. K.; Portner, J.; Coropceanu, I.; Das, A.; Tasone, C. J.; Teitelbaum, S. W.; Limmer, D. T.; Talapin, D. V.; Ginsberg, N. S. In Situ X-ray Scattering Reveals Coarsening Rates of Superlattices Self-Assembled from Electrostatically Stabilized Metal Nanocrystals Depend Nonmonotonically on Driving Force. *ACS Nano* **2024**, *18*, 5778–5789, Publisher: American Chemical Society.
- (58) Percus, J. K.; Yevick, G. J. Analysis of Classical Statistical Mechanics by Means of Collective Coordinates. *Physical Review* **1958**, *110*, 1–13, Publisher: American Physical Society.
- (59) Wertheim, M. S. Exact Solution of the Percus-Yevick Integral Equation for Hard Spheres. *Physical Review Letters* **1963**, *10*, 321–323, Publisher: American Physical Society.

- (60) Kinning, D. J.; Thomas, E. L. Hard-sphere interactions between spherical domains in diblock copolymers. *Macromolecules* **1984**, *17*, 1712–1718.
- (61) Dallari, F.; Reiser, M.; Lokteva, I.; Jain, A.; Möller, J.; Scholz, M.; Madsen, A.; Grübel, G.; Perakis, F.; Lehmkuhler, F. Analysis Strategies for MHz XPCS at the European XFEL. *Applied Sciences* **2021**, *11*, 8037, Number: 17 Publisher: Multidisciplinary Digital Publishing Institute.
- (62) Thompson, A. P.; Aktulga, H. M.; Berger, R.; Bolintineanu, D. S.; Brown, W. M.; Crozier, P. S.; in 't Veld, P. J.; Kohlmeyer, A.; Moore, S. G.; Nguyen, T. D.; Shan, R.; Stevens, M. J.; Tranchida, J.; Trott, C.; Plimpton, S. J. LAMMPS - a Flexible Simulation Tool for Particle-Based Materials Modeling at the Atomic, Meso, and Continuum Scales. *Computer Physics Communications* **2022**, *271*, 108171.